Shock-induced collapse of a vapor nanobubble near solid boundaries

Francesco Magaletti, Mirko Gallo, Luca Marino, Carlo Massimo Casciola*

Dipartimento di Ingegneria Meccanica e Aerospaziale, Università di Roma "La Sapienza", via Eudossiana 18, 00184 Roma, Italy

ARTICLE INFO

ABSTRACT

The collapse of a nano-bubble near a solid wall is addressed here exploiting a phase field model recently used to describe the process in free space. Bubble collapse is triggered by a normal shock wave in the liquid. The dynamics is explored for different bubble wall normal distances and triggering shock intensities. Overall the dynamics is characterized by a sequence of collapses and rebounds of the pure vapor bubble accompanied by the emission of shock waves in the liquid. The shocks are reflected by the wall to impinge back on the re-expanding bubble. The presence of the wall and the impinging shock wave break the symmetry of the system, leading, for sufficiently strong intensity of the incoming shock wave, to the poration of the bubble and the formation of an annular structure and a liquid jet. Intense peaks of pressure and temperatures are found also at the wall, confirming that the strong localized loading combined with the jet impinging the wall is a potential source of substrate damage induced by the cavitation.

1. Introduction

The collapse of vapor bubbles near solid boundaries has been deeply investigated in the last century. The triggering episode goes back to the finding of the destructive effects of cavitation phenomena on the propellers of the great ocean liners at the beginning of the 20th century. Similar effects have been observed successively on the blade of big hydraulic machines like turbines and pumps (Silberrad, 1912; Leighton, 2012). Only recently, due to the increasing impact of the micro and nano-technologies, the attention from millimeter-size bubbles has shifted downwards, toward micro or sub-micro bubbles. Indeed in microfluidic devices, the so called *lab on a chip*, cavitation phenomena can be employed for microfluidic pumping (Dijkink and Ohl, 2008), to enhance mixing by means of vorticity generation during the final stage of bubble collapse and for surface cleaning purposes (Ohl et al., 2006). Cavitation bubbles are also used in advanced medical procedures like high intensity focused ultrasound (HIFU) and extracorporeal shock wave lithotripsy (ESWL) (Coussios and Roy, 2008) to enhance drug delivery or increase local heat deposition deep within the body, to control localized cell membrane poration (Sankin et al., 2010), and to comminute kidney stones (Zhu et al., 2002). Moreover, the use of femtosecond lasers, generating nanometric bubbles, has recently

found important applications in nanosurgery of cells and tissues (Vogel et al., 2005; 2008).

The experimental investigation has played the most important part in the understanding of bubble–wall interactions, so far. The improvements in the bubble generation techniques led to cleaner and better reproducible data, starting from the kinetic impulse technique (Benjamin and Ellis, 1966). This approach suffers from the disadvantage that the bubble must be located before the application of the impulse. Successively the problem of localization has been overcome by means of the generation of the bubble by using an electric spark (Naudé and Ellis, 1961; Tomita and Shima, 1986). As a drawback, the electrodes perturb the bubble motion in the last stage of the collapse. At the moment, the best bubble generation technique is, probably, the non-intrusive pulsed-laser discharge (Vogel et al., 1989) that can focus an intense local heating and vaporization of the liquid through application of a thermal impulse. The visualization of the bubble dynamics can be performed by illuminating the scene with diffuse backlighting (Blake and Gibson, 1981) and by means of high-speed cameras, up to 20 million frames per second (Ohl et al., 1995). More recently, the μ-PIV technique has been used to measure the flow field during the bubble collapse (Sankin et al., 2010). The experiments allowed the visualization of the jet formation during the bubble collapse near solid surfaces and the assessment of the role of shock-wave emission, jet-wall interaction and chemical effects on cavitation damage (Benjamin and Ellis, 1966; Plesset and Ellis, 1955). Notwithstanding the extreme frame-rate of modern cameras, the complete and detailed description of thermo-acoustic and

flow fields, is still lacking. The temperature and pressure inside the bubble at the collapse instant is not easily accessible with non-intrusive measurements. The pressure indeed can be only extrapolated by measuring it with an hydrophone at some distance from the bubble and by assuming a classical $1/r$ decay (Lauterborn and Vogel, 2013). The temperature instead can be estimated by matching a blackbody radiation with the measured spectrum of the emitted light upon collapse (Flannigan and Suslick, 2005).

On the other hand, the mathematical modeling of cavitation is still a great challenge. The cornerstone in the theory of bubble dynamics was the pioneering work of Rayleigh (1917) who described the collapse of a bubble immersed in a unbounded incompressible liquid. Despite the significant simplifying assumptions, the correspondence with experimental results is still impressive. The model has been successively refined by taking into account compressibility effects in the liquid (Keller and Kolodner, 1956; Hickling and Plesset, 1964) and the presence of a dilute gas in the bubble. These refined models provided an estimate of the pressure peaks reached inside the bubble on the order of hundred times the pressure of the liquid environment. Numerical simulations and more complex analysis followed (Plesset and Chapman, 1971; Plesset and Prosperetti, 1977; Shima and Sato, 1981) in order to describe the effect of a nearby boundary. Different numerical techniques have been used in order to capture the interfacial dynamics, ranging from the Boundary Element Method (BEM) for irrotational conditions (Blake and Gibson, 1981) to the Arbitrary Lagrangian Eulerian (ALE) schemes (Tipton et al., 1992; Ding and Gracewski, 1996). Recently more sophisticated models have been proposed to gain new insights on the effects of dissolved gas and phase change (Akhatov et al., 2001) and to obtain a deeper knowledge in fascinating phenomena like sonoluminescence (Brenner et al., 2002). Of particular interest is the diffuse interface approach which enables a natural description of interfacial flows, changes of topology, vapor/liquid and vapor/supercritical fluid phase changes which have been shown to be crucial for the correct description of the final stages of the bubble collapse (Magaletti et al., 2015).

In this work we will exploit the diffuse interface model to numerically investigate the collapse of a sub-micron vapor bubble near solid boundaries. The effect of the initial bubble–wall distance will be analyzed and the visualization of the entire flow and thermo-acoustic fields will be provided. Particular attention will be paid to the stress distribution on the solid wall and we will address the role of the different pressure waves on cavitation damage.

The paper is organized as follows: in Section 2 the diffuse interface model and the relevant conservation equations is derived; Section 3 provides details on the numerical scheme and describes the numerical setting of the simulations; finally, the results of the numerical experiments will be discussed in Section 4 to finally draw conclusions and provide final comments in the last Section 5.

2. Mathematical model

Thermodynamics of non-homogeneous systems

We exploit an unsteady diffuse interface description (Anderson et al., 1998) of the multiphase flow in a domain $\mathcal{D}$ based on the van der Waals gradient approximation of the free energy functional $F[\rho, \theta]$ (Dell'Isola et al., 1995; Jamet et al., 2001):

$$F[\rho, \theta] = \int_{\mathcal{D}} \hat{f} dV = \int_{\mathcal{D}} \left(\hat{f}_0(\rho, \theta) + \frac{\lambda}{2} |\nabla \rho|^2 \right) dV, \tag{1}$$

where $\hat{f} = \hat{f}_0 + \lambda/2 |\nabla \rho|^2$ with $\hat{f}_0(\rho, \theta)$ the classical Helmholtz free energy density per unit volume of the homogeneous fluid at temperature θ and mass density ρ. The coefficient $\lambda(\rho, \theta)$, in general function of the thermodynamic state, embodies all the information on the interfacial properties of the liquid–vapor system (i.e.

surface tension and interface thickness). In particular, for a van der Waals fluid, the free energy reads

$$\hat{f}_0(\rho, \theta) = \bar{R}\rho\theta \left[-1 + \log \left(\frac{\rho K \theta^{1/\delta}}{1 - b\rho} \right) \right] - a\rho^2, \tag{2}$$

with $\delta = \bar{R}/c_v$, $\bar{R}$ the gas constant, c_v the constant volume specific heat, a and b the van der Waals coefficients and K a constant related to the de Broglie length (Zhao et al., 2011).

Equilibrium conditions

The present paragraph summarizes, for the reader convenience, results concerning thermodynamic equilibrium for systems described by the free energy functional (1). Although well known to specialists, we deemed useful to present a short summary to rationalize this classical material which is hardly described comprehensively in literature, Jamet (1998).

At given temperature, equilibrium is characterized by the minimum of the free energy functional in Eq. (1), where variations are performed with respect to the density distribution ρ. The evaluation of the functional derivative leads to the following equilibrium condition:

$$\mu_c^0 - \nabla \cdot \left(\lambda \nabla \rho \right) = const, \tag{3}$$

where the temperature is constrained to be constant, $\theta = const$, and $\mu_c^0 = \partial \hat{f}_0 / \partial \rho |_\theta$ is the classical chemical potential. The equation defines a generalized chemical potential $\mu_c = \mu_c^0 - \nabla \cdot \left(\lambda \nabla \rho \right)$ that must be constant at equilibrium.

The consequence of the above equilibrium conditions is better illustrated in the simple case of a planar interface, where the only direction of inhomogeneity is x, under the assumption of constant λ. The constant temperature appears in the equilibrium problem as a parameter and will not be further mentioned throughout the present section. Hence, determining the equilibrium density distribution amounts to finding a solution of

$$\mu_c = \mu_c^0(\rho) - \lambda d^2\rho/dx^2 = \mu_{eq}, \tag{4}$$

where the chemical potential in the bulk fluid (the vapor phase, say), far from the interface where $d\rho/dx = 0$, determines the constant $\mu_{eq} = \mu_c^0(\rho_V) = \mu_c^0(\rho_L)$. By multiplying Eq. (4) by $d\rho/dx$ and integrating between $\rho_\infty = \rho_V$ and ρ, leads to

$$\hat{w}_0(\rho) - \hat{w}_0(\rho_V) = \frac{\lambda}{2} \left(\frac{d\rho}{dx} \right)^2, \tag{5}$$

where $\hat{w}_0(\rho) = \hat{f}_0(\rho) - \mu_{eq}\rho$. Eq. (5) shows that $\hat{w}_0$ has the same value in both the bulk phases, where the spatial derivative of mass density vanishes: $\hat{w}_0(\rho_L) = \hat{w}_0(\rho_V)$.

The grand potential, defined as the Legendre transform of the free energy,

$$\Omega = F - \int_{\mathcal{D}} \rho \frac{\delta F}{\delta \rho} dV = \int_{\mathcal{D}} \hat{w} dV, \tag{6}$$

has the density (*actual* grand potential density)

$$\hat{w}[\rho] = \hat{f} - \mu_c \rho = \hat{f}_0 + \frac{\lambda}{2} \left(\frac{d\rho}{dx} \right)^2 - \left(\mu_c^0 - \lambda \frac{d^2\rho}{dx^2} \right) \rho, \tag{7}$$

implying that, in the bulk, $\hat{w} = \hat{w}_0$, i.e. $\hat{w}_0$ is the *bulk* grand potential density.

Given the form of $\hat{w}_0(\rho)$, the solution of Eq. (5) provides the equilibrium density profile $\rho(x)$:

$$x = \sqrt{\frac{\lambda}{2}} \int_{\rho_v}^{\rho} \frac{d\rho}{\sqrt{w_0(\rho) - w_0(\rho_V)}} + const. \tag{8}$$

Eq. (8) provides the equilibrium density profile characterized by two bulk regions separated by a thin layer. The layer thickness can be estimated as

$$\epsilon = \frac{\rho_L - \rho_V}{d\rho/dx|_{max}}. \tag{9}$$

The equilibrium condition, Eq. (5), provides the interface thickness in terms of the *bulk* grand potential density $\hat{w}_0(\rho)$ and of the parameter λ,

$$\epsilon = (\rho_L - \rho_V)\sqrt{\frac{\lambda}{2[\hat{w}_0(\bar{\rho}) - \hat{w}_0(\rho_V)]}}, \tag{10}$$

without explicitly addressing the density profile. $\bar{\rho}$ is the density corresponding to the maximum of $d\rho/dx$, achieved where $d\hat{w}_0/d\rho = 0$, Eq. (5).

The surface tension can be defined as the excess (*actual*) grand potential density,

$$\sigma = \int_{-\infty}^{x_i} \left(\hat{w}[\rho] - \hat{w}[\rho_V]\right)dx + \int_{x_i}^{\infty} \left(\hat{w}[\rho] - \hat{w}[\rho_L]\right)dx$$
$$= \int_{-\infty}^{\infty} \left(\hat{w}[\rho] - \hat{w}[\rho_V]\right)dx, \tag{11}$$

where x_i is the position of the Gibbs dividing surface, whose precise value is not influential since $\hat{w}[\rho_V] = \hat{w}[\rho_L]$ (we stress that, e.g., $\hat{w}[\rho_V]$ should be interpreted as the functional (7) evaluated on the constant density ρ_V). Given the definition of $\hat{w}[\rho]$, Eq. (7), and exploiting the equilibrium condition for the chemical potential, Eq. (4), it follows that

$$\sigma = \int_{-\infty}^{\infty} \left[\hat{f}_0 + \frac{1}{2}\lambda\left(\frac{d\rho}{dx}\right)^2 - \mu_{eq}\rho - \hat{w}_0(\rho_V)\right]dx$$
$$= \int_{-\infty}^{\infty} \left[\hat{w}_0 + \frac{1}{2}\lambda\left(\frac{d\rho}{dx}\right)^2 - \hat{w}_0(\rho_V)\right]dx. \tag{12}$$

Using Eq. (5) one finds

$$\sigma = \int_{-\infty}^{+\infty} \lambda\left(\frac{d\rho}{dx}\right)^2 dx = \int_{\rho_V}^{\rho_L} \lambda\frac{d\rho}{dx}d\rho$$
$$= \int_{\rho_V}^{\rho_L} \sqrt{2\lambda\left(\hat{w}_0(\rho) - \hat{w}_0(\rho_V)\right)}\,d\rho, \tag{13}$$

where the second expression can be evaluated with no *a priori* knowledge of the equilibrium density profile. We observe that, as for the interface thickness, the surface tension only depends on the form of the *bulk* grand potential density $\hat{w}_0(\rho)$ in the density range between the two equilibrium values, $[\rho_V; \rho_L]$, and on the parameter λ.

Eq. (5) applied to the two bulk regions where $d\rho/dx = 0$ implies the mechanical equilibrium condition $p_0(\rho_L) = p_0(\rho_V)$, where

$$p_0 = -\frac{\partial f_0}{\partial v} = -\frac{\partial \hat{f}_0/\rho}{\partial v} = \rho\mu_c^0 - \hat{f}_0 \tag{14}$$

is the classical thermodynamic pressure, $f_0 = \hat{f}_0/\rho$ the specific bulk free energy, and $v = 1/\rho$ the specific volume. Indeed Eq. (5) implies $\hat{w}_0(\rho_V) = \hat{w}_0(\rho_L)$, which corresponds to the equality of the pressures given that $p_0 = -\hat{w}_0$.

Equations of motion

The dynamics of the inhomogeneous system is described by the conservation equations for mass ρ, momentum $\rho\mathbf{u}$, and total energy E densities of

$$\frac{\partial \rho}{\partial t} + \nabla \cdot (\rho\mathbf{u}) = 0, \tag{15}$$

$$\frac{\partial \rho\mathbf{u}}{\partial t} + \nabla \cdot (\rho\mathbf{u} \otimes \mathbf{u}) = \nabla \cdot \boldsymbol{\tau}, \tag{16}$$

$$\frac{\partial E}{\partial t} + \nabla \cdot (\mathbf{u}E) = \nabla \cdot [\boldsymbol{\tau} \cdot \mathbf{u} - \mathbf{q}_e]. \tag{17}$$

The system (15–17) needs to be complemented with thermodynamically consistent constitutive relations for the stress tensor $\boldsymbol{\tau}$ and the energy flux $\mathbf{q}_e$. Their derivation is outlined below for the simplest case of constant λ, following the general approach for non-equilibrium processes described in De Groot and Mazur (2013).

It is instrumental to rewrite the energy equation in terms of specific internal energy $\mathcal{U}$, obtained by subtracting the equation for the kinetic energy from Eq. (17)

$$\rho\frac{D\mathcal{U}}{Dt} = \boldsymbol{\tau} : \nabla\mathbf{u} - \nabla \cdot \mathbf{q}_e, \tag{18}$$

where $D/Dt = \partial/\partial t + \mathbf{u} \cdot \nabla$ is the material derivative. By definition $\mathcal{U} = f + \theta\eta$, with $f = \hat{f}/\rho$ the specific Helmholtz free energy and η the specific entropy. The total derivative of $\mathcal{U}$ reads

$$d\mathcal{U} = \frac{\partial f}{\partial \rho}d\rho + \frac{\partial f}{\partial \nabla\rho} \cdot d\nabla\rho + \theta d\eta. \tag{19}$$

The partial derivatives of the specific free energy can be derived from its definition, Eq. (1), and from the definition of the thermodynamic pressure, Eq. (14). Explicitly, one finds

$$\frac{D\mathcal{U}}{Dt} = \frac{1}{\rho^2}\left(p_0 - \frac{\lambda}{2}|\nabla\rho|^2\right)\frac{D\rho}{Dt}$$
$$+ \theta\frac{D\eta}{Dt} + \frac{\lambda}{\rho}\nabla\rho \cdot \frac{D\nabla\rho}{Dt}. \tag{20}$$

The material derivative of the density gradient (last term in the RHS of Eq. (20)) can be evaluated by applying the gradient operator to the equation of mass conservation, Eq. (15):

$$\frac{\lambda}{\rho}\nabla\rho \cdot \frac{D\nabla\rho}{Dt} = -\frac{\lambda}{\rho}\nabla\rho \cdot \nabla\left(\rho\nabla \cdot \mathbf{u}\right) - \frac{\lambda}{\rho}\nabla\rho \otimes \nabla\rho : \nabla\mathbf{u}. \tag{21}$$

After substitution of Eqs. (15), (20), (21) into Eq. (18), a few more elementary manipulations allow to write the evolution equation for the entropy as

$$\rho\frac{D\eta}{Dt} = \nabla \cdot \left(\frac{\lambda\rho\nabla\rho\nabla \cdot \mathbf{u} - \mathbf{q}_e}{\theta}\right)$$
$$+ \frac{1}{\theta^2}[\lambda\rho\nabla\rho\nabla \cdot \mathbf{u} - \mathbf{q}_e] \cdot \nabla\theta$$
$$+ \frac{1}{\theta}\left[\boldsymbol{\tau} + \left(p_0 - \frac{\lambda}{2}|\nabla\rho|^2 - \rho\nabla \cdot \left(\lambda\nabla\rho\right)\right)\boldsymbol{I}\right.$$
$$\left.\lambda\nabla\rho \otimes \nabla\rho\right] : \nabla\mathbf{u}. \tag{22}$$

The term under divergence defines the entropy flux. Since the entropy production must be positive definite in terms of the thermodynamic forces (Clausius-Duhem inequality), the other two contributions on the right hand side are required to be positive. Assuming linear dependence of thermodynamic fluxes – terms in square brackets in (22) – on thermodynamic forces – $\nabla\theta$ and $\nabla\mathbf{u}$ – leads to identify the stress tensor with the following expression,

$$\boldsymbol{\tau} = -p_0\boldsymbol{I} + \boldsymbol{\Sigma}$$
$$= \left(-p_0 + \frac{\lambda}{2}|\nabla\rho|^2 + \rho\nabla \cdot \left(\lambda\nabla\rho\right)\right)\boldsymbol{I}$$
$$- \lambda\nabla\rho \otimes \nabla\rho$$
$$+ \mu\left[\left(\nabla\mathbf{u} + \nabla\mathbf{u}^T\right) - \frac{2}{3}\nabla \cdot u\boldsymbol{I}\right], \tag{23}$$

where the usual viscous terms with $\mu > 0$ in the last line are the source of mechanical irreversibility (for the sake of simplicity we have assumed the second viscosity coefficient equal to $-2\mu/3$). Concerning the energy flux, positive entropy production, second line in Eq. (22), calls for

$$\mathbf{q_e} = \lambda\rho\boldsymbol{\nabla}\rho\boldsymbol{\nabla}\cdot\mathbf{u} - k\boldsymbol{\nabla}\theta, \tag{24}$$

where $k > 0$ is the thermal conductivity.

Hereafter we assume constant values for μ and k and we adopt the van der Waals free energy density $\hat{f}_0$, Eq. (2), to obtain

$$p_0 = \bar{R}\frac{\rho\theta}{1 - b\rho} - a\rho^2, \tag{25}$$

$$\mathcal{U} = \frac{\bar{R}}{\delta}\theta - a\rho + \frac{\lambda}{2\rho}|\boldsymbol{\nabla}\rho|^2, \tag{26}$$

where the last term corresponds to the capillary contribution to the internal energy, $\mathcal{U}_c = \frac{\lambda}{2\rho}|\boldsymbol{\nabla}\rho|^2$.

Dimensionless parameters

By introducing the dimensionless (or reduced) variables

$$\rho^* = \rho/\rho_c, \qquad p^* = p/p_c, \qquad \theta^* = \theta/\theta_c,$$

where

$$\rho_c = \frac{1}{3b}, \qquad p_c = \frac{a}{27b^2}, \qquad \theta_c = \frac{8a}{27\bar{R}b}$$

are the critical values of density, pressure and temperature, respectively, the caloric and thermal equations of state take the form

$$E^* = \frac{8}{3\delta}\rho^*\theta^* - 3\rho^{*2} + \frac{1}{2}\rho^*|\mathbf{u}^*|^2 + \frac{1}{2}\mathcal{C}|\boldsymbol{\nabla}^*\rho^*|^2, \tag{27}$$

$$p_0^* = \frac{8\theta^*\rho^*}{3 - \rho^*} - 3\rho^{*2}, \tag{28}$$

where $u_R = \sqrt{p_c/\rho_c}$ is a reference velocity and L_R is a reference length. Time is made dimensionless with respect to the reference time $t_R = L_R/u_R$. $\mathcal{C} = \lambda\rho_c^2/(p_c L_R^2)$ is a dimensionless parameter quantifying the relevance of capillary stress to the dynamics.

For the reader's convenience, the constitutive laws are rewritten in dimensionless variables to highlight the relevant control parameters. The asterisk ($*$) is hereafter suppressed for the ease of notation:

$$\boldsymbol{\tau} = \left(-p_0 + \frac{\mathcal{C}}{2}|\boldsymbol{\nabla}\rho|^2 + \mathcal{C}\rho\nabla^2\rho\right)\boldsymbol{I} - \mathcal{C}\,\boldsymbol{\nabla}\rho\otimes\boldsymbol{\nabla}\rho$$
$$+ \frac{1}{Re}\left[(\boldsymbol{\nabla}\mathbf{u} + \boldsymbol{\nabla}\mathbf{u}^T) - \frac{2}{3}\boldsymbol{\nabla}\cdot u\boldsymbol{I}\right], \tag{29}$$

$$\mathbf{q_e} = \mathcal{C}\,\rho\boldsymbol{\nabla}\rho\boldsymbol{\nabla}\cdot\mathbf{u} - \frac{1}{Re\,Pr}\boldsymbol{\nabla}\theta. \tag{30}$$

$Re = L_R\sqrt{p_c\rho_c}/\mu$ is a Reynolds number based on critical quantities and $Pr = 3\mu\bar{R}/(8k)$ is the analogous for a van der Waals fluid of the familiar Prandtl number.

3. Algorithms and solution techniques

The numerical solution of the system of equations (15–17) is challenging due to a combination of different physical phenomena, which all require a specialized numerical technique.

Apart from the extremely thin liquid–vapor interface that requires a high numerical resolution, the system supports i) the propagation of shock waves; ii) viscous diffusion and capillary dispersion; iii) phase change and transition to and from supercritical conditions.
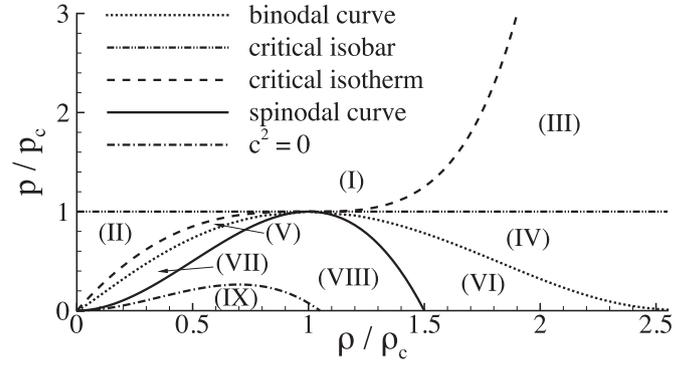
Fig. 1. Phase diagram in the $p - \rho$ plane. In the zone (I) where $p > p_c$ and $\theta > \theta_c$ the fluid is in supercritical state. Zone (II), characterized by $p < p_c$ but $\theta > \theta_c$, is the gas region. Conversely, zone (III) where $p > p_c$ but $\theta < \theta_c$ is the compressible-liquid region. In zone (IV) and (V) the fluid is in liquid or vapor state, respectively. Under the binodal curve, which represent the saturation conditions, we find zones (VI) and (VII) of metastable liquid and metastable vapor state, respectively. The spinodal curve, defined as $\partial p/\partial\rho|_\theta = 0$, separates the metastable regions from the unstable region (VIII). Finally, in subset of the unstable region, zone (IX), $c^2 = \partial p/\partial\rho|_\eta < 0$, i.e. the sound speed becomes imaginary.

From a numerical point of view, compressibility and shock wave propagation would suggest the adoption of specialized shock-capturing methods, like the Essentially Non Oscillatory schemes, or their Weighted WENO extension (Shu, 1998). However hyperbolic features conflict with the diffusive and dispersive behavior induced by viscosity and capillarity. Moreover, at least for the van der Waals equation of state, (28), a region of the thermodynamic phase space exists where $\partial p_0/\partial\rho|_\eta < 0$. As well known, in ordinary conditions, this derivative defines the square of the sound speed, implying that where $c^2 < 0$ hyperbolic behavior changes into parabolic, see Fig. 1 for an explanatory diagram. The strategy conceived to deal with this complex mathematical structure, is based on two basic ingredients: 1) Identification of the hyperbolic part of the operator and its extension to the parabolic region where $c^2 < 0$; 2) Operator splitting into hyperbolic and non-hyperbolic part. For convenience, these two ingredients will be discussed in reverse order.

Operator splitting

As discussed in Section 2, the state of the system is identified by three basic, conserved fields, namely mass, momentum and total energy density, to be collectively addressed here as the state vector $\mathbf{U}(\mathbf{x}, t) = (\rho, \rho\mathbf{u}, E)^T$. Formally system (15–17) can be written as

$$\frac{\partial\mathbf{U}}{\partial t} = \mathcal{N}[\mathbf{U}] = \mathcal{H}_e[\mathbf{U}] + \mathcal{P}[\mathbf{U}],$$

where $\mathcal{H}_e$ is the extension to the whole phase space of the hyperbolic part of the operator and $\mathcal{P} = \mathcal{N} - \mathcal{H}_e$ is defined accordingly. The explicit expressions of the two operators $\mathcal{H}_e$ and $\mathcal{P}$ will be provided below. After the operator is split as explained, the state vector can be evolved in time exploiting a solution strategy in terms of Strang splitting (Strang, 1968). Denoting $F_\mathcal{N}(t)$ the full propagator such that

$$\mathbf{U}(t + \tau) = F_\mathcal{N}(\tau)\mathbf{U}(t),$$

for small τ we can approximate

$$F_\mathcal{N}(\tau) = F_\mathcal{P}(\tau/4)F_{\mathcal{H}_e}(\tau/2)F_\mathcal{P}(\tau/4)$$

where $F_\mathcal{P}(\tau)$ is the propagator of system

$$\frac{\partial\mathbf{U}}{\partial t} = \mathcal{P}[\mathbf{U}],$$

while $F_{\mathcal{H}_e}(\tau)$ is defined by

$$\frac{\partial \mathbf{U}}{\partial t} = \mathcal{H}_e[\mathbf{U}].$$

Strang splitting allows for using different algorithms, specialized for each component of the system. The algorithms we selected are a third order WENO (Shu, 1998) scheme for the hyperbolic part and a second order accurate, centered finite difference scheme for the parabolic part. We performed the time integration of the hyperbolic part with a full explicit, third-order TVD Runge–Kutta scheme. The parabolic operator is advanced in time with a mixed, implicit-explicit scheme, where the linear terms (viscous stress and heat flux) are treated implicitly in order to increase the stability limit.

Definition of the operators above the binodal

In the region of phase space where the sound speed is well defined, the hyperbolic step is

$$\frac{\partial \rho}{\partial t} = -\nabla \cdot (\rho \mathbf{u}), \tag{31}$$

$$\frac{\partial \rho \mathbf{u}}{\partial t} = -\nabla \cdot (\rho \mathbf{u} \otimes \mathbf{u} + p_0 \mathbf{I}), \tag{32}$$

$$\frac{\partial E_0}{\partial t} = -\nabla \cdot [\mathbf{u}(E_0 + p_0)] - \frac{\partial (\rho \mathcal{U}_c)}{\partial t}. \tag{33}$$

where $E_0 = \rho(\mathcal{U}_0 + 1/2|\mathbf{u}|^2)$ is the total energy density deprived of the capillary contribution, which reproduces the classical Euler equation. The capillary contribution to the energy ($\rho \mathcal{U}_c$) is treated as an explicit forcing term depending on the density gradient. Here, as already stated, a van der Waals fluid is assumed in the equations of state. The parabolic part of the operator corresponds to

$$\frac{\partial \rho}{\partial t} = 0, \tag{34}$$

$$\frac{\partial \rho \mathbf{u}}{\partial t} = \nabla \cdot \mathbf{\Sigma}, \tag{35}$$

$$\frac{\partial E}{\partial t} = \nabla \cdot \left(-\frac{1}{2}\lambda |\nabla \rho|^2 \mathbf{u} + \mathbf{\Sigma} \cdot \mathbf{u} - \mathbf{q}_e\right), \tag{36}$$

where the capillary contribution (first term in the right hand side of the equation for E) has been included in the energy flux.

Definition of the operators below the binodal

In the coexistence region below the binodal (or coexistence curve, Fig. 1), which contains the region where $c^2 < 0$, a Maxwell-like rule is used. Using the additivity of specific volume and entropy, mass density and specific entropy can be written as

$$\frac{1}{\rho} = (1 - \alpha)\frac{1}{\rho_V(\theta)} + \alpha \frac{1}{\rho_L(\theta)}$$

$$\eta_{sat} = (1 - \alpha)\eta_V(\theta) + \alpha \eta_L(\theta)$$

where subscript L and V denote pure liquid and vapor at the given temperature. The above relations can be inverted to yield

$$\alpha = \alpha(\rho, \eta_{sat})$$

$$\theta = \theta(\rho, \eta_{sat}).$$

For the mixture of vapor and liquid, the saturation pressure depends only on temperature, such that

$$p_{sat} = p_{sat}(\theta) = p_{sat}(\rho, \eta_{sat}).$$

This expression allows to extract the sound speed as

$$c_{sat}^2 = \frac{\partial p_{sat}}{\partial \rho}\bigg|_{\eta_{sat}} > 0$$

whose final expression is

$$c_{sat}^2 = \frac{\left(\dfrac{d p_{sat}}{d\theta}\right)^2}{\rho^2 \left(\dfrac{d\eta_L}{d\theta} + \dfrac{1}{\rho_L^2}\dfrac{d p_{sat}}{d\theta}\dfrac{d\rho_L}{d\theta} - \dfrac{\rho - \rho_L}{\rho \rho_L}\dfrac{d^2 p_{sat}}{d\theta^2}\right)}. \tag{37}$$

The interested reader is referred to Michaelides and Zissis (1983) for details on the thermodynamic derivation of the sound speed for the mixture.

In fact, the actual pressure differs from the saturation pressure,

$$p_0 = p_0(\theta, \rho) = p_{sat}(\theta) + \delta p(\theta, \rho),$$

to the extent that $c^2 = \partial p / \partial \rho|_\eta$ may become negative. We stress however that $c_{sat}^2 > 0$, thereby allowing to identify the hyperbolic part of the evolution operator in the region below the binodal (which includes the region where $c^2 < 0$).

Concerning the energy density, we consistently address the energy of the liquid–vapor mixture,

$$E_{sat} = 1/2 \rho |\mathbf{u}|^2 + \rho[(1 - \alpha)\mathcal{U}_V + \alpha \mathcal{U}_L].$$

Again, the actual energy is

$$E = E_{sat} + \delta E.$$

With the above position, the split system in the region below the binodal reads

$$\frac{\partial \rho}{\partial t} = -\nabla \cdot (\rho \mathbf{u}), \tag{38}$$

$$\frac{\partial \rho \mathbf{u}}{\partial t} = -\nabla \cdot (\rho \mathbf{u} \otimes \mathbf{u} + p_{sat} \mathbf{I}), \tag{39}$$

$$\frac{\partial E_{sat}}{\partial t} = -\nabla \cdot [\mathbf{u}(E_{sat} + p_{sat})] - \frac{\partial \delta E}{\partial t}, \tag{40}$$

for the hyperbolic part and

$$\frac{\partial \rho}{\partial t} = 0, \tag{41}$$

$$\frac{\partial \rho \mathbf{u}}{\partial t} = -\nabla \delta p + \nabla \cdot \mathbf{\Sigma}, \tag{42}$$

$$\frac{\partial E}{\partial t} = \nabla \cdot [-\mathbf{u}(\delta E + \delta p) + \mathbf{\Sigma} \cdot \mathbf{u} - \mathbf{q}_e], \tag{43}$$

for the parabolic part, respectively.

We stress that the definitions of the operators given separately for the two regions of phase space join continuously at the binodal curve.

Thermodynamic state of the liquid–vapor mixture

Concerning the thermodynamics of the homogeneous vapor–liquid mixture below the binodal, the saturation densities $\rho_V(\theta)$ and $\rho_L(\theta)$, are evaluated as follows. Given the state of the system in terms of density and temperature, the corresponding chemical potential is

$$\mu_c^0 = \frac{8}{3}\theta \left[\frac{\rho}{3 - \rho} - \log\left(\frac{K(3 - \rho)\theta^{1/\delta}}{3\rho}\right)\right] - 6\rho. \tag{44}$$
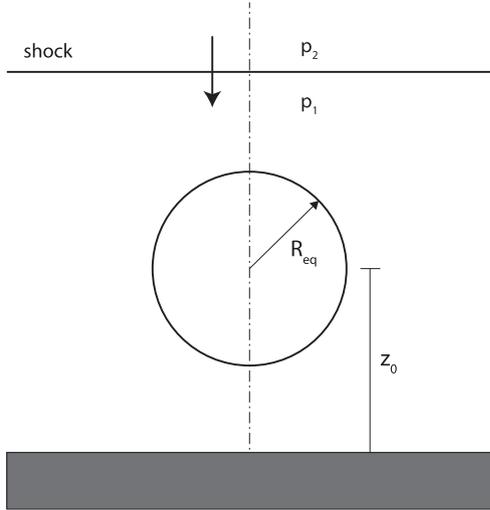
Fig. 2. Sketch of the simulation setup.

Fig. 3. Time evolution of the bubble volume for different initial wall–bubble distance z_0. The initial distance does not substantially affect the bubble dynamic during the first collapse, indeed the collapse time remains unaltered in all the numerical experiments. The characteristic frequency of collapse and re-expansion is not a function of the initial position. Conversely, the dynamic of the re-expansion and of the successive collapses is influenced by the initial position in a nontrivial way. In the inset it is reported the comparison between the shock-induced collapse near a wall (the solid red curve, $z_0 = 1.3$) and in free space (dotted black curve) where the bubble does not experience a volume plateau after the collapse. (For interpretation of references to color in this figure legend, the reader is referred to the web version of this article.)

Chemical, thermal and mechanical equilibrium require equality of temperature, $\theta_V = \theta_L = \theta$, pressure, $p_V = p_L$, and chemical potential $\mu_V^0 = \mu_L^0$. After some algebra, one ends up with the following non-linear 2×2 system for ρ_L and ρ_V

$$\frac{8\theta\rho_L}{3 - \rho_L} - 3\rho_L^2 = \frac{8\theta\rho_V}{3 - \rho_V} - 3\rho_V^2,$$

$$\theta\left[\frac{3(\rho_L - \rho_V)}{(3 - \rho_L)(3 - \rho_V)} + \log\left(\frac{\rho_L(3 - \rho_V)}{\rho_V(3 - \rho_L)}\right)\right]$$
$$= \frac{9}{4}(\rho_L - \rho_V),$$

which is solved by a standard Newton algorithm.

Simulations setup

All the simulations have been performed using an axisymmetric code, exploiting cylindrical symmetry, see the sketch in Fig. 2. The system is initialized with a vapor bubble of radius R_{eq} centered in z_0, the distance between the wall and the bubble center. The effect of the initial distance is analyzed by performing 5 simulations at different z_0. The vapor bubble is in equilibrium with the confining liquid at temperature $\theta/\theta_c = 0.6$. A shock wave with intensity $I = (p_2 - p_1)/p_1$, with p_2 and p_1 the pressure in the perturbed and the unperturbed state, respectively, is initialized to hit the bubble and trigger the collapse. In most of the results to be discussed, $I = 75$. A further case at $I = 400$ is also considered, to highlight the destabilizing effect of the impinging shock intensity. The fluid domain has dimension $4R_{eq} \times 4R_{eq}$ and has been discretized with a uniform grid 2048×2048. The mesh influence has been analyzed by comparing the bubble evolution on a coarser mesh, 1024×1024. Since the results are nearly indistinguishable, only those obtained with the finer mesh has been produced here since the accuracy, in particular during the final stage of the collapse, is expected to be slightly better. An adaptive timestep, ranging from 10^{-5} down to 10^{-8}, has been used during the simulations to comply with stability and accuracy requirements. In particular, the smaller ones are used during the collapse stage, when the shockwaves are formed, in order to follow the large and fast changes experienced by the field. Selecting $L_R = R_{eq}$, the dimensionless parameters of the simulations are: $Re = 50$, $Pr = 0.2$ and $\mathcal{C} = 1.6 \times 10^{-4}$. These values correspond, e.g., to a bubble radius order of $100\,\text{nm}$ with typical viscosity, thermal conductivity, surface tension and critical values of water.

4. Results and discussions

Overall, the dynamics of the bubble is characterized by a sequence of rebounds, as shown by the plots of bubble volume vs. time reported in Fig. 3 for different wall normal distances of the bubble and for the triggering shock strength $I = 75$. Generically, the first collapse phase (volume decreasing in time), is only slightly affected by the initial wall distance. After the minimum volume is reached, a plateau is observed. It will be shown to be related to the interaction of the bubble with the shock wave which is emitted when the collapse is arrested and is successively reflected back by the wall. After the shock/bubble interaction is completed, the bubble starts expanding up to a maximum volume, which is systematically lower than the initial value. The process ends with the full condensation of the bubble.

Equilibrium vapor bubble

Before discussing in detail the actual dynamics observed in the simulations, it may be instrumental to identify the effect of a compression on an equilibrium bubble. Given the temperature, a system formed by a vapor bubble in equilibrium with the liquid should satisfy the conditions of constant chemical potential, Eq. (4),

$$\mu_c^0(\rho_L, \theta) = \mu_{eq}$$
$$\mu_c^0(\rho_V, \theta) = \mu_{eq},$$

where the equilibrium state is parametrized by θ and μ_{eq}, and the chemical potential for a van der Waals fluid is explicitly provided in Eq. (44).

The equilibrium conditions are described in Fig. 4, where a constant chemical potential line, thin solid line, is plotted in the $\rho - p$ plane. An isotherm is also reported as a red solid line. The intersection of the two curves determines three points in the plane. The
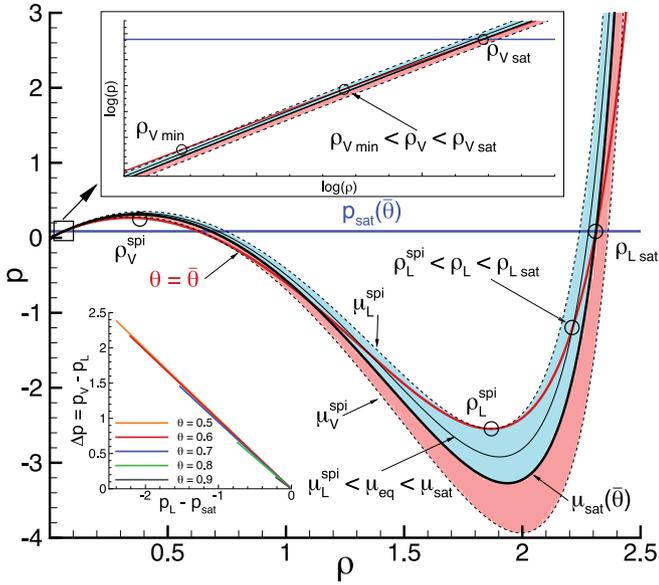
Fig. 4. Illustration of the iso-chemical potential (black curves), isotherm (red curve, $\bar{\theta} = 0.6$) and isobar (blue curve) for a van der Waals equation of state in the ρ–p plane. The range of very low densities is enlarged in the top inset. The equilibrium properties (same chemical potential, temperature and pressure) identify the saturation densities (ρ_{Vsat} and ρ_{Lsat}) as the intersection of the iso-chemical potential μ_{sat} (thicker black curve) and the isotherm and isobar. The two colored regions span the chemical potential values where a vapor bubble (light blue) or a liquid drop (light red) can be found as a metastable equilibrium condition for the fluid system. In the bottom inset the effect of reducing the liquid pressure, p_L, under the saturation value on the equilibrium pressure difference, Δp, between the vapor bubble and the external liquid, is plotted for different fixed temperatures. The corresponding bubble radius can be obtained by the classical Young–Laplace equation. (For interpretation of references to color in this figure legend, the reader is referred to the web version of this article.)

low density one corresponds to the vapor, ρ_V, p_V, and is hardly visible on the scale of the plot, see the enlargement on the upper part of the figure. The intersection at largest density corresponds to the liquid, ρ_L, p_L. The third intersection, at intermediate density $\rho_V^{spi}(\theta) < \rho_{un} < \rho_L^{spi}(\theta)$, always belongs to the unstable region of the phase space, below the spinodal, see Fig. 1. The region of the phase space where the above three intersections exist is shown by the colored band in the figure. More specifically, denoted by $\mu_L^{spi}(\theta)$ and $\mu_V^{spi}(\theta)$ the chemical potential at the liquid and vapor spinodal, the condition $\mu_L^{spi}(\theta) < \mu_{eq} < \mu_V^{spi}(\theta)$ defines the relevant range of chemical potential. Outside the colored band, only one intersection is found, corresponding to vapor or liquid, according to the condition $\mu_{eq} < \mu_L^{spi}$ or $\mu_{eq} > \mu_V^{spi}$, respectively.

The pressure, of the vapor, say, is recovered from the pressure equation of state (25), in combination with the expression for the chemical potential Eq. (44), to yield $p_V = p_V(\mu_{eq}, \theta)$. The chemical potential at saturation, black thick line in Fig. 4, is such that $p_V(\mu_{sat}, \theta) = p_L(\mu_{sat}, \theta) = p_{sat}(\theta)$. As a property of the solution, $p_L \lessgtr p_V$ when $\mu_{eq} \lessgtr \mu_{sat}$. It follows that, in order to have a bubble ($p_V > p_L$), the chemical potential must be smaller than the saturation value, $\mu_L^{spi} < \mu_{eq} < \mu_{sat}$, light blue band in Fig. 4. In this case the vapor is stable (i.e. the vapor point is above the binodal) and the liquid is metastable (liquid between binodal and spinodal). The other case, $\mu_V^{spi} > \mu_{eq} > \mu_{sat}$, corresponds to a drop of stable liquid in metastable vapor (light red band in the figure).

By inverting the relationship $p_L = p_L(\mu_{eq}, \theta)$ and inserting it in the expression for vapor pressure, $p_V = p_V(\mu_{eq}, \theta)$, allows to express the pressure difference between vapor and liquid as a function of the liquid pressure,

$$\Delta p = p_V - p_L = f(p_L, \theta),$$

where $\Delta p > 0$ (vapor bubble) when $p_L < p_{sat}$. This relation, illustrated in the lower inset of Fig. 4 for several temperatures, is hardly distinguishable from a straight line on the adopted scale. Since $\mu_L^{spi} < \mu_{eq} < \mu_{sat}$, the corresponding range of liquid pressure is $p_L^{spi} < p_L < p_{sat}(\theta)$, where p_L^{spi} is the pressure at the liquid spinodal. When the liquid pressure belongs to the allotted interval, the equilibrium radius of the bubble can then be estimated by using the Young–Laplace equation, $R_{eq} = 2\sigma/\Delta p$ (the exact solution requires solving the corresponding problem in the phase field context Dell'Isola et al., 1995).

Let us consider the bubble–liquid system in equilibrium with a given pressure p_L in the liquid. Assume the liquid is now compressed to a new state, $p_L' = p_L + \delta p_L$. If the compression is such that $p_L' < p_{sat}$, the bubble will find a new equilibrium condition, with a new pressure p_V' and a new radius R_{eq}'. A counterintuitive effect is that, under compression of the liquid, the radius of the new equilibrium bubble increases. This is opposite to the behavior expected from a gas bubble, and is explained by the inset of Fig. 4 where the pressure jump across the interface is shown to be a decreasing function of the liquid pressure. A little more though immediately provides the clue for understanding this behavior. In fact, increasing the pressure, the liquid gets closer to saturation conditions, implying that also the vapor inside the bubble approaches saturation, see the inset of Fig. 4. The consequence is that the pressure difference Δp between vapor and liquid decreases, leading to a larger equilibrium radius as a consequence of the Young–Laplace equation.

If the compression exceeds the saturation pressure, no vapor bubble can exist in equilibrium with the compressed liquid: in this case the vapor condenses altogether, and the new equilibrium state corresponds to a single phase, pure liquid. Our interest here is focused on the nonequilibrium process that leads to such eventual condensation, when the compression is associated to a shock wave in the liquid impinging the vapor bubble. In order to achieve full condensation the shock wave amplitude $p_2 - p_1$ should be larger than $p_{sat} - p_1$, i.e. $I > p_{sat}/p_1 - 1$, where p_1 is the liquid pressure in equilibrium with the initial vapor bubble.

Non-equilibrium process

Experiments on laser induced bubbles in water (Noack and Vogel, 1998) show that energy deposition by a focused laser beam leads to a fast local vaporization and the compression of the liquid. By measuring the speed of the shock wave, the authors could find the intensity of the shock wave as a function of the energy of the laser pulse. It is found that pressures in excess of 10 GPa are easily excited in water at standard conditions. Clearly the strength of the shock wave decreases with the distance from the focusing point, confirming that almost planar waves can easily be generated in the liquid with the intensity we are using here to trigger the collapse of the bubble ($I \in [75, 400]$).

The evolution of the vapor bubble is represented in Figs. 5 and 6 for two different initial wall distances, $z_0 = 1.3$ and $z_0 = 1.9$, respectively. The weak impinging shockwave and the proximity of the wall is not sufficient to immediately break the spherical symmetry and to produce the classical liquid jet that porates the bubble, clearly observed in millimeter-bubble experiments (Benjamin and Ellis, 1966; Lauterborn and Bolle, 1975; Ohl et al., 2006). At sub-micron scale the surface tension is, in fact, predominant and preserves the nearly spherical shape during the first part of the evolution. Symmetry breaking eventually occurs when the bubble shrinks to its minimum volume and a non-spherical shockwave is emitted. By comparing Figs. 5 and 6, the asymmetry is stronger for the bubble closer to the wall, where, instead of being more or less spherical, the shockwave produced at collapse consists of two curved shock fronts that propagate toward and away from
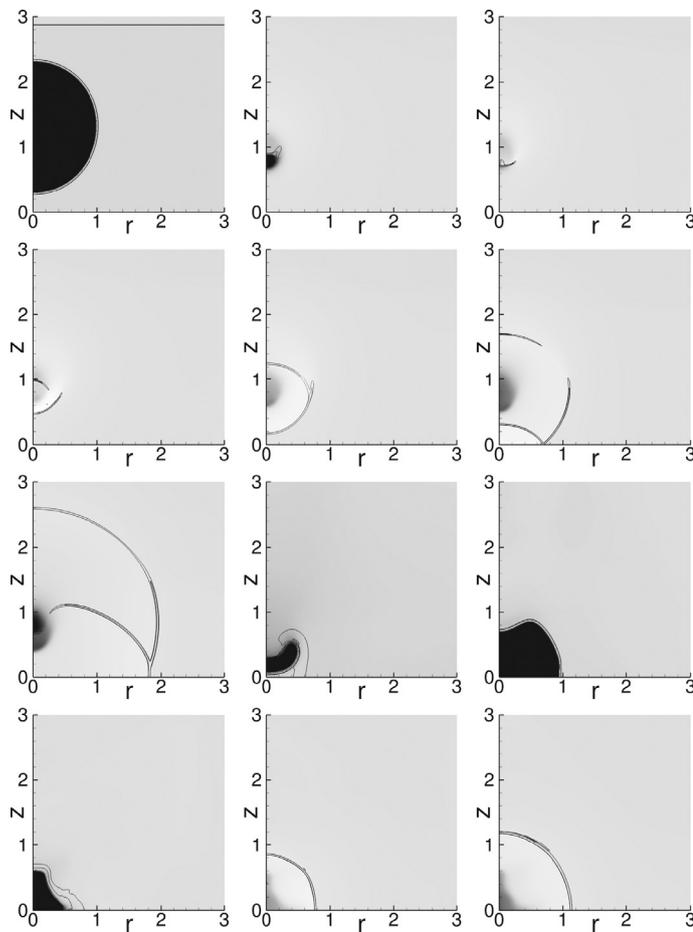
Fig. 5. Snapshots during the evolution of a collapsing bubble with $z_0 = 1.3$. The sequence runs from left to right and from top to bottom and is not uniformly spaced in time ($t = 0, 2.237, 2.261, 2.28, 2.316, 2.376, 2.527, 4.152, 6.407, 7.474, 7.683, 7.736$). The grey tones from darker to lighter represent the density field from smaller (vapor phase) to higher (liquid phase). The black lines are Schlieren-like iso-lines obtained as $S = \exp(-|\nabla p_0|/|\nabla p_0|_{max})$. The drawn iso-levels are $S = 0.9$ and $S = 1$ in order to highlight the regions with the highest pressure gradients, i.e. the vapor–liquid interface and the shockwaves.

Fig. 6. Snapshots during the evolution of a collapsing bubble with $z_0 = 1.9$ taken at times $t = 0, 2.266, 2.319, 2.395, 2.399, 2.771, 4.545, 4.627, 7.04, 7.533, 7.736, 9.482$. The grey tones and the iso-lines are the same of Fig. 5.

the wall. The former is eventually reflected by the solid wall and strikes again the re-expanding bubble. During this stage the bubble becomes flatter (elongated in the radial direction) and moves toward the wall. The expansion stage is strongly affected by the bubble–wall distance, with the closest bubble (Fig. 5) touching the wall and the farthest one (e.g. in Fig. 6) remaining detached. During the bubble expansion, the liquid in the thin layer between vapor and wall is compressed and a new shockwave is observed, third row of Fig. 6. This sequence of events completely breaks the spherical symmetry, thereby reducing the strength of the successive collapse. Eventually, the field becomes more and more complex, until dissipation prevails. It is worth noting that, at a qualitative level, the configuration of the shock waves compares very well with results found in experiments in similar conditions, Tomita and Shima (1986). It should be stressed however that in the experiments the bubble is usually much larger, typically millimeter size. However femtosecond lasers allow to generate nano-sized bubbles, see Vogel et al. (2008).

Increasing the strength of the impinging shockwave, liquid-jet formation is observed. In Fig. 7 the evolution of the vapor bubble triggered by a shockwave of intensity $I = 400$ is represented up to the first re-expansion stage. The shape of the collapsing bubble becomes much flatter than observed at weaker shock strengths and the strong vorticity generated at the periphery of the bubble gives

rise to the bubble poration by inducing a liquid jet focused toward the wall. In the third row of Fig. 7, during the re-expansion stage, the bubble acquires an annular shape and the liquid jet impinges the wall and produces a radial flow.

A direct comparison of the flow induced by the bubble collapse at different strengths of the triggering shockwave is reported in Fig. 8. The liquid jet directed toward the wall is more pronounced for $I = 400$ and the flow is strong enough to pierce the bubble leading to an annular shape. In fact, although a wall-directed flow is observed also in the case of the weaker initial shockwave, at $I = 75$ the bubble is not flat enough to be pierced by the liquid jet and the overall effect reduces to a displacement of the bubble toward the wall.

A crucial aspects of the phenomenology is the transition to supercritical conditions during the last stage of the collapse (Magaletti et al., 2015). The formation of an incondensable phase prevents the complete collapse of the bubble, reverting the motion to an outward expansion. Overall, a sequence of oscillations sets in, as shown in Fig. 3, where the quantity reported on the ordinate is the volume of the non-liquid phase in the system (vapor and supercritical phases). During each successive collapse, the vapor is compressed and its temperature raises locally bringing the system in supercritical conditions. As already anticipated, Fig. 3, the volume during the first collapse stage is almost independent of the bubble–wall distance. On the contrary, the re-expansion stage is affected by the initial position. The following dynamics is affected by the complex interactions between the reflected shockwaves and the bubble motion. The time of the successive collapses are slightly
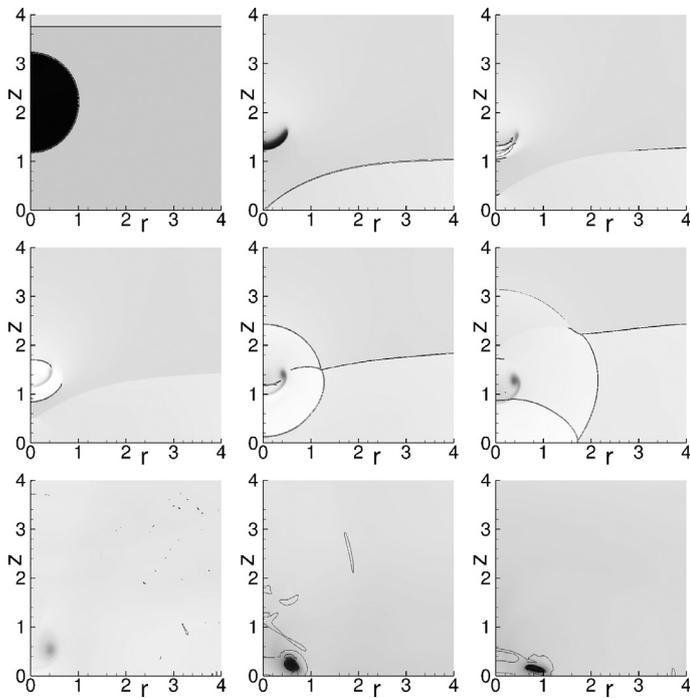
Fig. 7. Snapshots during the evolution of a collapsing bubble with $z_0 = 2.2$ and a trigger shockwave with intensity $I = 400$. The time instants correspond to $t = 0, 0.948, 0.985, 1.007, 1.068, 1.156, 1.766, 2.36, 2.822$. The grey tones and the isolines are the same of Fig. 5. The stronger impinging shock initiates the liquid jet formation and leads to the bubble poration.
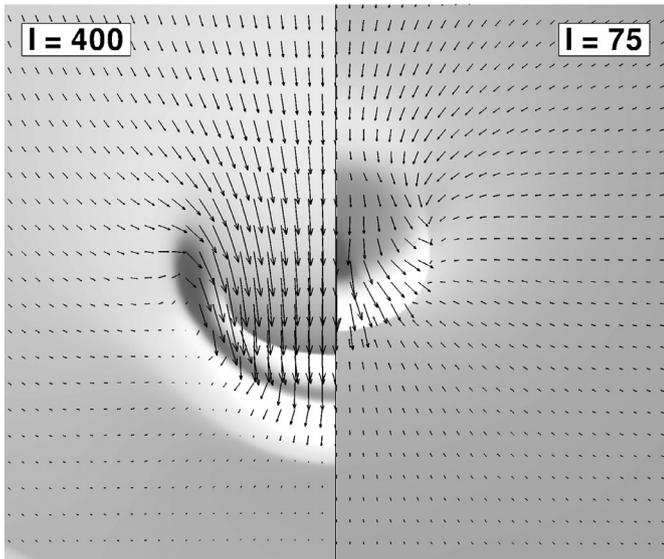
Fig. 8. Comparison of the flow fields for two different shock intensities. On the left the case $I = 400$ where it is apparent the liquid jet formation. On the right the case $I = 75$. The plotted vectors are not at the maximum grid resolution to increase the clearness of the figure.

Fig. 9. Time evolution of eccentricity for different initial distance. The first stage of the collapse is substantially spherical for all the initial distances. The break of symmetry occurs during the final stage of the collapse with the nearest bubble (red curve in the online version) that slightly extends toward the wall while the others in the radial direction. During the shock-interaction stage all the bubbles assumes a pronounced flat shape and remains elongated in the radial direction through all the re-expansion phase. The more drastic change of topology occurs during the second collapse when all the bubbles rapidly invert the elongation toward the wall. (For interpretation of references to color in this figure legend, the reader is referred to the web version of this article.)
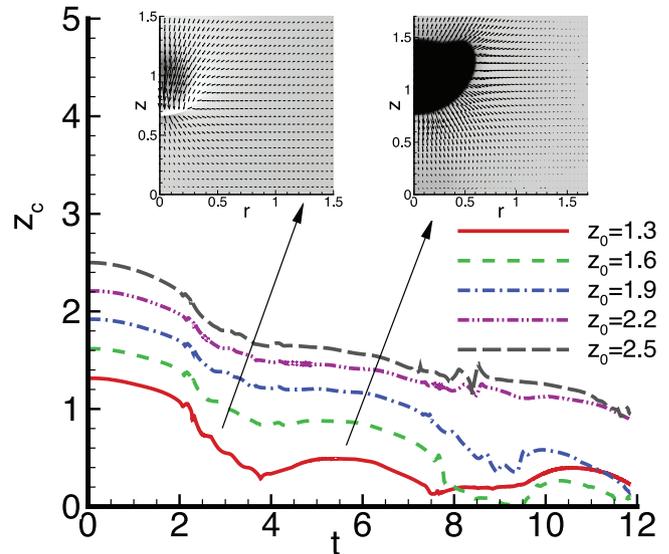
Fig. 10. Evolution of the position of the bubble center. The faster migration toward the wall occurs between the collapse and the re-expansion stages when the flow produced during the bubble collapse is stronger and convects the bubble. The two snapshots in the insets show the velocity vectors in two different stages: on the left it is highlighted the axial flow during the bubble migration, while on the right it is shown the characteristic quasi-radial flow during the re-expansion phase that stops the axial motion of the bubble.

different for the different cases (differences up to 10%) and the maximum volume achieved after the second re-expansion is not monotonous with z_0. In the inset of Fig. 3 we compare the volume evolution of a shock-induced collapse in free space (black dotted curve) with the one near the wall (red solid curve, $z_0 = 1.3$). The overall dynamics is again a series of collapses and rebounds but, after each collapse, the bubble in free space does not experience the volume plateau which is an effect of the interaction between the re-expanding bubble and the shockwave reflected back by the

wall. The reflected shock counteracts the re-expansion and keeps the bubble small for a longer time.

The eccentricity of the bubble, $e = a/b$, where a is the semi-axis in the z-direction and b is the other semi-axis of the ellipsoid with the same volume of the bubble, $V = 4\pi ab^2/3$, can be used to quantify the change in bubble shape, with $e < 1$ for a flat bubble (elongated in the radial direction). The time evolution of the eccentricity is reported in Fig. 9, for several initial distances z_0.
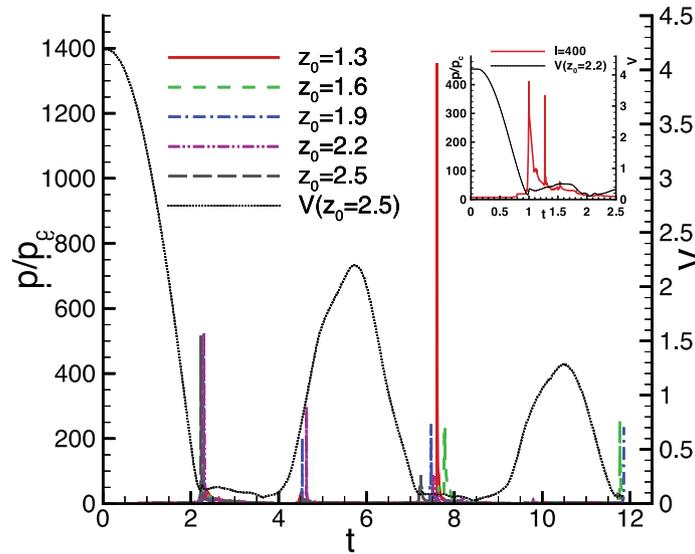
Fig. 11. Time evolution of the maximum pressure recorded in the whole fluid domain for the five different initial wall–bubble distances. As a reference the dotted curve reports the bubble volume evolution. The most intense pressure peaks are observed when the bubble reaches its minimum volume. In the case of $z_0 = 1.3$, the maximum value is reached at the second collapse because the bubble is pinned on the solid boundary and its collapse is more intense. Of particular interest are the pressure peaks observed during the re-expansion stage for the cases $z_0 = 1.6$ and $z_0 = 2.2$ which are related to the compression of the liquid film between the bubble and the wall, as explained in the text. In the inset we report the time evolution of the maximum pressure in the case with the higher triggering shock intensity.

Let us focus on the first collapse stage. As anticipated, during the initial phase of the first collapse, all the bubbles remain almost spherical. The initial distance affects, instead, the shape in the final part of the collapse in such a way that the farther bubbles take a flatter shape ($e < 1$) while the closer ones get slightly elongated toward the wall ($e > 1$). This trend is the consequence of two counteracting effects of the triggering shockwave. On one hand the impinging shock flattens the bubble during the collapse. On the other hand the bubble-shock interaction weakens the pressure wave and slows it down locally in the region occupied by the bubble (see the second and third snapshots in the first row of Fig. 7). Its reflection at the wall produces a non-uniform shockwave impinging again the bubble. The reflected shock is now more intense on the sides than on the center of the bubble thereby enhancing the elongation in the z-direction. The effect is clearly more intense for bubbles closer to the wall.

After the first collapse, up to the re-expansion stage, all the bubbles flatten as a consequence of the radial flow occurring near the wall. The second collapse is characterized by a rapid reduction of the radial semi-axis b (see the third and the forth rows of Fig. 6) and therefore by a quick increase of the eccentricity as a consequence of the local high curvature at the equator of the bubble in association with surface tension.

The flow produced during the bubble collapse and the consequent bubble motion is investigated in Fig. 10 showing the position of bubble center of mass, z_c. A strong axial flow, clearly visible in the inset on the left, is produced near the bubble axis during the collapse stage. This flow is responsible for the bubble migration toward the wall after the collapse ($t > 2$). Overall, despite the difference in lengthscale, the observed phenomenology is entirely consistent with the experimental observations on millimeter bubbles reported in Philipp and Lauterborn (1998). During the re-expansion stage the flow is directed radially outward (inset on the right), stopping the bubble motion toward the wall. The subsequent collapse regenerates the axial flow and the bubble approaches the wall again.

Shockwaves and jets formed during bubble collapse are associated with intense pressure and temperature peaks. At each time instant maximum pressure and temperature are recorded and reported in the plots of Fig. 11 and 12, respectively. The first peak,
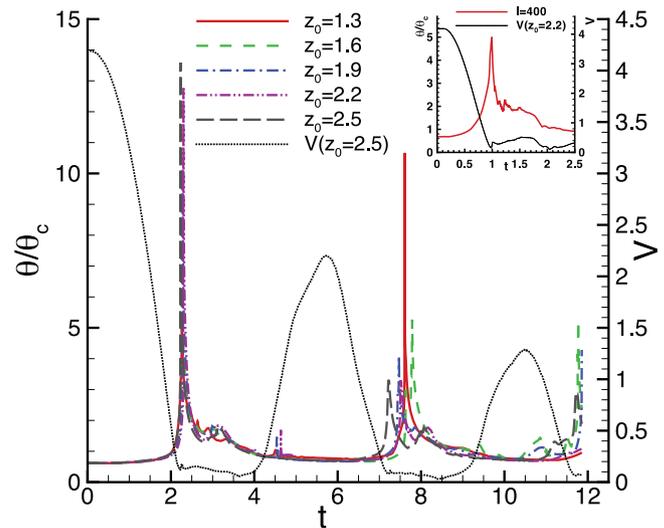
Fig. 12. Time evolution of maximum temperature recorded in the whole fluid domain. As well as the pressure peaks, the temperature reaches the local maxima when the collapse is completed. Again, it is possible to observe a temperature peak during the re-expansion stage, but it is less apparent than its pressure equivalent. In the inset we report the time evolution of the maximum pressure in the case $l = 400$.

both in pressure and temperature, occurs at the end of the first collapse stage, when the bubble stops shrinking. This peak is the strongest one for a bubble collapsing in free space (Magaletti et al., 2015). Fig. 11 shows that the end of the first collapse is the instant of maximum pressure also for most cases of bubbles collapsing near the wall. However there are conditions where a successive peak exceeds by far the first one. When it occurs, such extremely intense pressure peak is due to the bubble experiencing the second collapse after it translated to get in touch with the wall, see the snapshots in the last row of Fig. 5. It may even happen that an intermediate pressure peak occurs between the first and
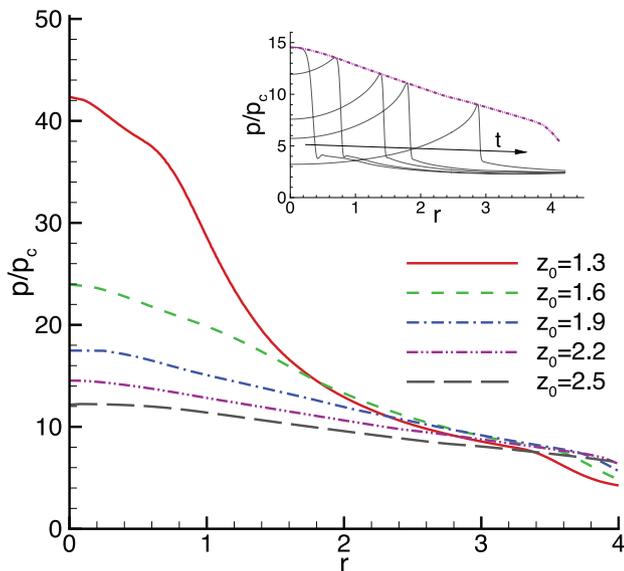
Fig. 13. Spatial evolution of the maximum pressure values recorded on the wall during propagation of the shock wave for each initial condition. The pressure values are decreasing with increasing of initial bubble distance from the wall. It is possible to observe that for the bubbles placed at distances closer to the wall the shape of the envelope varies strongly due to interaction with the shockwave reflection. Inset: Radial evolution of the pressure range recorded on the wall for initial condition $z_0 = 2.2$. The different dotted lines correspond to different time instants and the purple line corresponds to the envelope of the maximum pressure values. (For interpretation of references to color in this figure, the reader is referred to the web version of this article.)

the second collapse. When present, this is due to the expansion of the bubble at a suitable distance to the wall that generates a compression of the fluid between bubble and wall (third row of Fig. 6). As already commented, the increase in the triggering shock intensity leads to bubble poration and jet development. Interestingly, at the moment of jet formation, a peak in the pressure field is observed, inset of Fig. 11. The origin of the pressure peak is purely hydrodynamical, since no corresponding temperature peak occurs, see inset of Fig. 12. Since the jet-induced pressure peak is comparable with that of the shock, the present results seem to confirm the high damaging potential of the jetting phase.

The collapsing bubble induces a strong stress on the solid wall. Fig. 13 reports the envelope of the pressure maxima at the wall for different initial bubble positions. The inset illustrates the way the envelope is constructed from instantaneous pressure distributions at the wall at successive time instants. By comparing with the pressure maxima in the field, Fig. 11, it is clear that the pressure at the wall is much weaker than the maximum inside the field. Nevertheless the typical pressure at the wall is very large, order ten times the critical pressure of the fluid. For water, this would correspond to a pressure in the order of 200 MPa, a figure which compares well with experimental measurements on collapsing bubbles near solid walls (Tomita and Shima, 1986). Concerning the temperature at the wall, in the present conditions extreme values were never experienced, except in cases where the collapsing bubble came in direct contact with the wall.

5. Conclusions

We have numerically studied the collapse of a pure vapor nanobubble near a solid boundary by applying a diffuse interface approach. The model is especially suitable to describe in a consistent and unified way the complex phenomena occurring during cavitation, namely: phase change, latent heat release, shock wave formation and propagation, transition to supercritical conditions.

Table 1
Comparison of the maximum pressure and temperature reached during the first collapse in three different geometrical configurations. In all the cases the overpressure that triggers the collapse is of intensity $I = 75$. The data shown as representative of the shock induced collapse in proximity of the wall is referred to the case with $z_0 = 1.6$.

	p_{max}/p_c	θ_{max}/θ_c
Spherical	3×10^5	708
Shock induced – no wall	175.16	3.29
Shock induced – near wall	384	8.22

Like in the case of spherically symmetric collapse, a pure vapor bubble is found to collapse with a sequence of volume oscillations, associated to a sequence of successive collapses which are arrested and inverted by the formation of the incondensable, supercritical phase due to compression and latent heat release. In comparison with symmetric collapse, the peak pressures and temperature are significantly lower in the case of aspherical bubble collapse, see Table 1. Interestingly, the peak pressure for shock wave induced collapse in free space leads to even lower pressure and temperatures in comparison with those reached when the collapse is triggered near the wall. This indicates that the wall, by confining the radial expansion of the bubble and reflecting the triggering shock enhances the peak pressure level. Despite the pressure peak realized at the wall is significantly lower than the maxima found inside the field, still large level of stress is transferred to the wall, as potential source of damage. A strong jet is found when the triggering shock strength is sufficiently large. In fact, jet impingement on the wall is often quoted as a concurrent cause of material damage (Tomita and Shima, 1986).

It is worthwhile noting that the peak pressure and temperature levels obtained in the present simulations are expected to overestimate the experimental values. The reason is the simple equation of state used to make the computations more easily affordable. In particular, a pressure equation of state better suited to model a real fluid could help to reduce the peak temperature and pressure values. Moreover, unless extremely weak forcing is used to initiate the bubble collapse, the large temperatures reached inside the bubble are expected to lead to dissociation and ionization phenomena, which concur in substantially limiting the peak temperature.

A further aspect to be considered for future works is the presence of dissolved gas in the liquid to reproduce the condition of partially gas-filled cavitation bubbles that are more commonly found in applications.

References

Akhatov, I., Lindau, O., Topolnikov, A., Mettin, R., Vakhitova, N., Lauterborn, W., 2001. Collapse and rebound of a laser-induced cavitation bubble. Phys. Fluids 13 (10), 2805–2819.

Anderson, D., McFadden, G., Wheeler, A., 1998. Diffuse-interface methods in fluid mechanics. Annu. Rev. Fluid Mech. 30 (1), 139–165.

Benjamin, T.B., Ellis, A.T., 1966. The collapse of cavitation bubbles and the pressures thereby produced against solid boundaries. Philos. Trans. R. Soc. Lond. A 260 (1110), 221–240.

Blake, J.R., Gibson, D., 1981. Growth and collapse of a vapour cavity near a free surface. J. Fluid Mech. 111, 123–140.

Brenner, M.P., Hilgenfeldt, S., Lohse, D., 2002. Single-bubble sonoluminescence. Rev. Mod. Phys. 74 (2), 425.

Coussios, C.C., Roy, R.A., 2008. Applications of acoustics and cavitation to noninvasive therapy and drug delivery. Annu. Rev. Fluid Mech. 40, 395–420.

De Groot, S.R., Mazur, P., 2013. Non-Equilibrium Thermodynamics. Courier Dover Publications.

Dell'Isola, F., Gouin, H., Seppecher, P., et al., 1995. Radius and surface tension of microscopic bubbles by second gradient theory. Comptes Rendus Acad. Sci.ences-Series (IIB-Mech.) 320, 211–216.

Dijkink, R., Ohl, C.-D., 2008. Laser-induced cavitation based micropump. Lab Chip 8 (10), 1676–1681.

Ding, Z., Gracewski, S., 1996. The behaviour of a gas cavity impacted by a weak or strong shock wave. J. Fluid Mech. 309, 183–209.

Flannigan, D.J., Suslick, K.S., 2005. Plasma formation and temperature measurement during single-bubble cavitation. Nature 434 (7029), 52–55.

Hickling, R., Plesset, M.S., 1964. Collapse and rebound of a spherical bubble in water. Phys. Fluids (1958–1988) 7 (1), 7–14.

Jamet, D., 1998. Etude des Potentialités de la Théorie du Second Gradient Pour la Simulation Numérique Directe des Ecoulements Liquide–Vapeur avec Changement de Phase Ph.D. thesis.

Jamet, D., Lebaigue, O., Coutris, N., Delhaye, J., 2001. The second gradient method for the direct numerical simulation of liquid–vapor flows with phase change. J. Comput. Phys. 169 (2), 624–651.

Keller, J.B., Kolodner, I.I., 1956. Damping of underwater explosion bubble oscillations. J. Appl. Phys. 27 (10), 1152–1161.

Lauterborn, W., Bolle, H., 1975. Experimental investigations of cavitation-bubble collapse in the neighbourhood of a solid boundary. J. Fluid Mech. 72 (02), 391–399.

Lauterborn, W., Vogel, A., 2013. Shock wave emission by laser generated bubbles. In: Bubble Dynamics and Shock Waves. Springer, pp. 67–103.

Leighton, T., 2012. The Acoustic Bubble. Academic Press.

Magaletti, F., Marino, L., Casciola, C., 2015. Shock wave formation in the collapse of a vapor nanobubble. Phys. Rev. Lett. 114 (6), 064501.

Michaelides, E., Zissis, K., 1983. Velocity of sound in two-phase mixtures. Int. J. Heat Fluid Flow 4 (2), 79–84.

Naudé, C.F., Ellis, A.T., 1961. On the mechanism of cavitation damage by nonhemispherical cavities collapsing in contact with a solid boundary. J. Fluids Eng. 83 (4), 648–656.

Noack, J., Vogel, A., 1998. Single-shot spatially resolved characterization of laser-induced shock waves in water. Appl. Opt. 37 (19), 4092–4099.

Ohl, C.-D., Arora, M., Dijkink, R., Janve, V., Lohse, D., 2006. Surface cleaning from laser-induced cavitation bubbles. Appl. Phys. Lett. 89 (7), 074102.

Ohl, C.-D., Philipp, A., Lauterborn, W., 1995. Cavitation bubble collapse studied at 20 million frames per second. Ann. Phys. 507 (1), 26–34.

Philipp, A., Lauterborn, W., 1998. Cavitation erosion by single laser-produced bubbles. J. Fluid Mech. 361, 75–116.

Plesset, M., Ellis, A., 1955. On the mechanism of cavitation damage. Trans. ASME 77, 1055–1064.

Plesset, M.S., Chapman, R.B., 1971. Collapse of an initially spherical vapour cavity in the neighbourhood of a solid boundary. J. Fluid Mech. 47 (02), 283–290.

Plesset, M.S., Prosperetti, A., 1977. Bubble dynamics and cavitation. Annu. Rev. Fluid Mech. 9 (1), 145–185.

Rayleigh, L., 1917. Viii. on the pressure developed in a liquid during the collapse of a spherical cavity. Lond. Edinb. Dublin Philos. Mag. J. Sci. 34 (200), 94–98.

Sankin, G., Yuan, F., Zhong, P., 2010. Pulsating tandem microbubble for localized and directional single-cell membrane poration. Phys. Rev. Lett. 105 (7), 078101.

Shima, A., Sato, Y., 1981. The collapse of a spheroidal bubble near a solid wall. J. Mec. 20 (2), 253–271.

Shu, C.-W., 1998. Essentially Non-Oscillatory and Weighted Essentially Non-Oscillatory Schemes for Hyperbolic Conservation Laws. Springer.

Silberrad, D., 1912. Propeller erosion. Engineering 33–35.

Strang, G., 1968. On the construction and comparison of difference schemes. SIAM J. Numer. Anal. 5 (3), 506–517.

Tipton, R.E., Steinberg, D.J., Tomita, Y., 1992. Bubble expension and collapse near a rigid wall. JSME Int. J. 35 (1), 67–75.

Tomita, Y., Shima, A., 1986. Mechanisms of impulsive pressure generation and damage pit formation by bubble collapse. J. Fluid Mech. 169, 535–564.

Vogel, A., Lauterborn, W., Timm, R., 1989. Optical and acoustic investigations of the dynamics of laser-produced cavitation bubbles near a solid boundary. J. Fluid Mech. 206, 299–338.

Vogel, A., Linz, N., Freidank, S., Paltauf, G., 2008. Femtosecond-laser-induced nanocavitation in water: implications for optical breakdown threshold and cell surgery. Phys. Rev. Lett. 100 (3), 038102.

Vogel, A., Noack, J., Hüttman, G., Paltauf, G., 2005. Mechanisms of femtosecond laser nanosurgery of cells and tissues. Appl. Phys. B 81 (8), 1015–1047.

Zhao, N., Mentrelli, A., Ruggeri, T., Sugiyama, M., 2011. Admissible shock waves and shock-induced phase transitions in a van der waals fluid. Phys. Fluids 23, 086101.

Zhu, S., Cocks, F.H., Preminger, G.M., Zhong, P., 2002. The role of stress waves and cavitation in stone comminution in shock wave lithotripsy. Ultrasound Med. Biol. 28 (5), 661–671.